

Title No. 120-M48

# Examining Effect of Printing Directionality on Freezing-and-Thawing Response of Three-Dimensional-Printed Cement Paste

by R. M. Ghantous, A. Evseeva, B. Dickey, S. Gupta, A. Prihar, H. S. Esmaeeli, R. Moini, and W. J. Weiss

*The use of three-dimensional (3-D) printing with cementitious materials is increasing in the construction industry. Limited information exists on the freezing-and-thawing (FT) performance of the 3-D-printed elements. A few studies have used standard FT testing procedures (ASTM C666) to assess the FT response; however, ASTM C666 is insensitive to anisotropy caused by printing directionality. This paper investigates the FT response of 3-D-printed cement paste elements using thermomechanical analysis (TMA) to examine the influence of directionality in comparison to cast counterparts. Cement paste with a water-cement ratio (w/c) of 0.275 was used. The critical degree of saturation ( $DOS_{CR}$ ) as well as the coefficient of thermal expansion (COTE) were determined for specimens with varying degrees of saturation (DOS). Micro-computed tomography (micro-CT) was conducted to quantitatively understand the heterogeneities in the pore microstructure of 3-D-printed materials. For the specimens fabricated in this study, the COTE and  $DOS_{CR}$  are independent of the 3-D-printing directionality and were comparable to conventionally cast specimens. For samples at 100% saturation, the FT damage was higher in the 3-D-printed samples as compared to the cast samples. The use of a low w/c in the 3-D-printed materials, desired from a buildability perspective, led to low capillary porosity, which thus decreased the amount of freezable pore solution and increased the FT resistance of the 3-D-printed materials. Micro-CT analysis demonstrated a significant 4.6 times higher average porosity in the interfacial regions compared to the filament cores.*

**Keywords:** anisotropy; coefficient of thermal expansion (COTE); freezable solution; freezing-and-thawing (FT) performance; three-dimensional (3-D)-printed cement paste.

## INTRODUCTION

There have been growing advancements in the fabrication of concrete elements made using additive manufacturing.<sup>1-8</sup> Additive manufacturing fabrication may improve productivity in the construction industry,<sup>9,10</sup> enable construction in remote areas using local materials,<sup>11</sup> reduce waste and costs associated with formwork,<sup>12</sup> and enable the creation of concrete components with complex architectures and novel performance.<sup>1,13,14</sup>

Studies have primarily focused on mixture designs and process development.<sup>15-21</sup> Other studies have examined the influence of processing parameters, such as speed and the time gap between the layers, on the mechanical properties of printed concrete specimens and on the interlayers' adhesion.<sup>14,19,22-26</sup> The durability of three-dimensional (3-D)-printed concrete structures is only recently being examined.<sup>27-35</sup> The layer-wise process of additive manufacturing

with cement-based materials may lead to microstructural heterogeneities such as weak interfaces.<sup>14,25,36</sup> Further research is necessary to understand whether 3-D-printed cement-based elements can be assumed to behave as a homogenous material with an isotropic material response.

This study will focus on one aspect of durability: the freezing-and-thawing (FT) response of printed cementitious materials. The presence of cold joints, macropores, and interfaces in the printed cementitious elements may influence their FT response.<sup>30,31,36</sup> In addition, the quality of the entrained air (that is, shape, size, and spacing), commonly used in conventional concrete to increase its FT resistance<sup>37,38</sup> may be altered due to the shearing process, the processing parameters such as extrusion pressure, and the interaction of air-entraining admixtures with other admixtures typically used in the mixture design of printed materials, such as high-range water-reducing admixtures (HRWRAs) and accelerators.<sup>35,39,40</sup>

Few studies have investigated the FT response of printed cementitious specimens.<sup>27,30,34,35,41,42</sup> Das et al.<sup>35</sup> used protected paste volume analysis to predict similar performance for the cast and printed specimens under freezing conditions. Das et al.<sup>30</sup> measured the FT resistance of printed and cast specimens using ASTM C666 Procedure B and concluded that printed specimens have lower resistance to FT cycles as compared to cast specimens due to high capillary porosity at the interface between the printed filaments.<sup>30</sup> Zhang et al.<sup>34</sup> measured higher FT damage in printed specimens as compared to cast samples using the dynamic elastic modulus; they concluded that the FT-induced damage occurred along weak printed interfaces, and the aggregates were more difficult to dislodge from the surface of printed specimens than cast samples due to the extrusion pressure leading to a densely packed surface in printed materials. Assaad et al.<sup>41</sup> concluded that the interface between filaments is more vulnerable to FT cycles as compared to the bulk of the printed mortar filaments. They observed that the rate of decrease in the interlayer bond was two to three times higher than the rate of decrease in the compressive and flexural strengths with the FT cycles.<sup>41</sup> Wangler et al.<sup>27</sup> showed the

*ACI Materials Journal*, V. 120, No. 4, July 2023.

MS No. M-2022-381.R1, doi: 10.14359/51738808, received March 26, 2023, and reviewed under Institute publication policies. Copyright © 2023, American Concrete Institute. All rights reserved, including the making of copies unless permission is obtained from the copyright proprietors. Pertinent discussion including author's closure, if any, will be published ten months from this journal's date if the discussion is received within four months of the paper's print publication.

first study on the field performance of printed cementitious materials exposed to an FT environment, where FT damage was assessed by a visual inspection of cracks development. Wang et al.<sup>42</sup> concluded that anisotropy influences the FT resistance of 3-D-printed mortar specimens.

The aforementioned studies evaluated the FT performance of 3-D-printed cementitious materials that were partially or fully immersed in water. However, an alternative approach, based on critical saturation theory, has been proposed to describe the FT response of conventional concrete by separately taking into account the water absorption and resistance of the specimen to freezing at a given degree of saturation (DOS).<sup>43-46</sup> The critical saturation theory states that concrete as a porous media is susceptible to FT damage only if its DOS is higher than a critical DOS level of saturation (that is,  $DOS > DOS_{CR}$ ). The time it takes concrete to reach the critical limit state ( $t_{CR}$ ) (that is, the onset of FT damage) can be computed using Eq. (1)<sup>47</sup>

$$DOS_{CR} = DOS_N + \dot{S}\sqrt{t_{CR} - t_N} \quad (1)$$

where  $DOS_N$  is the DOS where pores in the cement matrix are saturated<sup>48</sup>;  $\dot{S}$  is the rate of water absorption in a specimen after matrix pores have been filled (that is, filling of the air voids);  $t_N$  is the duration of time needed to reach  $DOS_N$  (typically a few days); and  $t_{CR}$  is the duration of time needed for the sample to reach critical saturation (ASTM C1585-13<sup>49</sup>).

For conventional concrete, it has been shown that the  $DOS_{CR}$  typically varies from 75 to 91% depending largely on the quality (the volume, size, and spacing) of the air-void system in concrete.<sup>46,50</sup>  $DOS_{CR}$  can be determined by measuring the FT damage in concrete at varying DOS from 100% to lower values at which no FT damage is detected.<sup>45,51</sup> The most common procedure consists of assessing the reduction in the dynamic modulus of elasticity by either using frequency measurements<sup>46,52</sup> or by using ultrasonic wave velocity measurements.<sup>53-55</sup> Length change can be used to assess  $DOS_{CR}$  for both cement paste and mortar specimens.<sup>56-59</sup> A residual change in dimension (that is, an increase in sample length) after a thermal cycle is an indicator of FT damage.<sup>56-59</sup> The thermomechanical analysis (TMA) measurements can be performed on specimens with various DOS and thus allow for the determination of  $DOS_{CR}$ .<sup>56-59</sup>

Previous TMA studies<sup>58,59</sup> examined cast specimens. This study investigates the influence of printing directionality on the FT response of 3-D-printed cement paste specimens, which encompass a heterogeneous microstructure with horizontal and vertical porous interfaces.<sup>25,36</sup> FT damage was measured using TMA in cast and printed specimens preconditioned to various DOS. This approach aims to determine whether microstructural heterogeneities and their directionality (interfaces parallel or perpendicular to the length of the specimen under investigation) influence the FT performance of printed elements at various levels of saturation. The coefficient of thermal expansion (COTE) is also extracted from this experimental data to assess any potential influence of layered heterogeneity and its directionality on the thermal expansion characteristics of 3-D-printed materials. This paper focuses on assessing “well-printed specimens” with

**Table 1—Properties of cement used in this study**

Cement oxides	Type I/II cement (OPC)
	Percentage by mass, %
Silicon dioxide (SiO <sub>2</sub> )	19.60
Aluminum oxide (Al <sub>2</sub> O <sub>3</sub> )	4.40
Ferric oxide (Fe <sub>2</sub> O <sub>3</sub> )	2.90
Calcium oxide (CaO)	60.70
Magnesium oxide (MgO)	3.70
Sulfur trioxide (SO <sub>3</sub> )	4.50
Equivalent alkali (Na <sub>2</sub> O <sub>eq</sub> )	0.75
Loss on ignition (LOI)	2.30
Bogue phase composition	Percentage by mass, %
Tricalcium silicate (C <sub>3</sub> S)	52.00
Dicalcium silicate (C <sub>2</sub> S)	17.00
Tricalcium aluminate (C <sub>3</sub> A)	7.00
Tetracalcium aluminoferrite (C <sub>4</sub> AF)	9.00
Specific gravity	3.15

a solid design of materials architecture (that is, “best-case scenario” specimens in which the filaments are printed close together with ~20% overlap and no intentional or few unintentional defects).

## RESEARCH SIGNIFICANCE

The FT performance of 3-D-printed elements is important as they are increasingly being developed in cold climates. Previous studies have examined 3-D-printed materials using test methods (ASTM C666) designed for conventional concrete. This paper examines the influence of printing directionality on the FT response of specimens with different DOS. The TMA test method is proposed and enables the FT response to be measured with respect to the printing direction.  $DOS_{CR}$  is evaluated for potential use in the critical saturation model. The influence of 3-D-printing direction is also evaluated for the COTE.

## EXPERIMENTAL PROCEDURE

### Materials and mixture design

A Type I/II ordinary portland cement (OPC) (ASTM C150-07)<sup>60</sup> was used in this study, and its chemical composition and physical properties can be found in Table 1. The Blaine fineness of the OPC used in this study was 412 m<sup>2</sup>/kg, and its fineness No. 325 sieve (passing) was 91.4%. An HRWRA and viscosity-modifying admixture (VMA) were used in this study (ASTM C494/C494M-08).<sup>61</sup> The water-cement ratio ( $w/c$ ) of the cement paste was 0.275. The mixture consisted of 250 g of cement, 1.47 g of HRWRA, 2.38 g of VMA, and 65.50 g of water.

### Mixture preparation, sample curing, and sample geometry

After weighing the materials, water was placed in the mixing bowl, then the VMA and HRWRA were added and dispersed using a spatula. Cement was then added to the liquid solution and mixed for 90 seconds at 400 revolutions

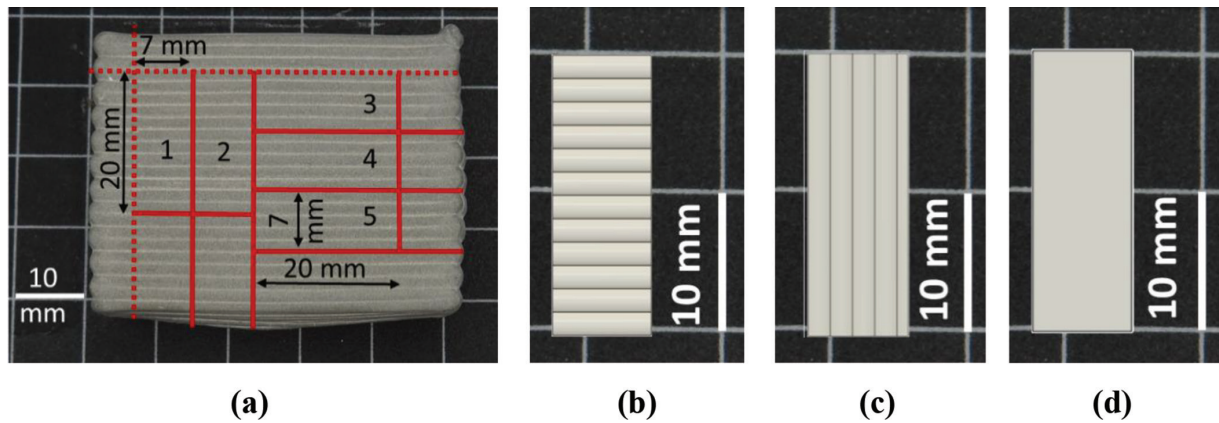


Fig. 1—(a) Cutting sample into smaller specimens for FT damage assessment using TMA for length change measurements. Schematic representation of three geometries tested in this study: (b) 3-D-printed solid lamellar specimens with filaments perpendicular to length change measurements; (c) 3-D-printed solid lamellar specimens with filaments parallel to length change measurements; and (d) specimen obtained from cast cement paste with no filaments and interfaces. Filaments are drawn at 1:1 scale.

per minute (rpm) in a programmable vacuum mixer at a 70% vacuum level. The vacuum was stopped for 15 seconds to scrape down in the mixing bowl any paste that may have collected on the side of the bowl. The cement paste was then mixed for an additional 90 seconds at 400 rpm at a 100% vacuum level. Further details of the mixing process can be found in the earlier work of the authors.<sup>21</sup>

The cast cement paste was prepared in 3-D-printed polylactic acid (PLA) rectangular molds of 50 x 40 x 12 mm.

For the preparation of the 3-D-printed cement paste samples with rectilinear (lamellar) architecture, the cement paste mixture was gradually filled in a 60 mL syringe into different layers, and each layer was manually consolidated to reduce the entrapped air. The syringe was then mounted on a stepper motor-driven extrusion system, which was connected to a 3-D printer.<sup>14</sup> A stainless-steel nozzle with an internal diameter of 1.36 mm was used in this study and was mounted to the printer using a customized nozzle holder. A polyethylene tube with an internal diameter of 4.3 mm and length of 450 mm was used to connect the syringe and the nozzle and ensure the transfer of the paste from the syringe to the nozzle.<sup>36</sup> The G-code commands for the 3-D printer were generated by the commercially available slicer using the dimensions of the prismatic sample (50 x 40 x 12 mm in length, width, and height), a solid infill (100%), a lamellar filament geometry, and suitable speed and extrusion printing parameters.<sup>25</sup> The printing speed of 750 mm/min (corresponding to a layer deposition time of 1.6 minutes) and the filament height of 1 mm were selected. The nominal width of the filament was 1.63 mm, which is 20% larger than the internal diameter of the nozzle due to the swelling of the extrudate known as the die-swell effect, which leads to approximately a 20% overlap between the filaments.

Both the cast and printed cement paste samples were transferred immediately after preparation to a sealed curing chamber that was maintained at  $93 \pm 2\%$  relative humidity (RH) using saturated solutions of potassium nitrate<sup>62</sup> according to the procedure introduced in Moini et al.<sup>36</sup> Twenty-four hours after printing, the specimens were sealed

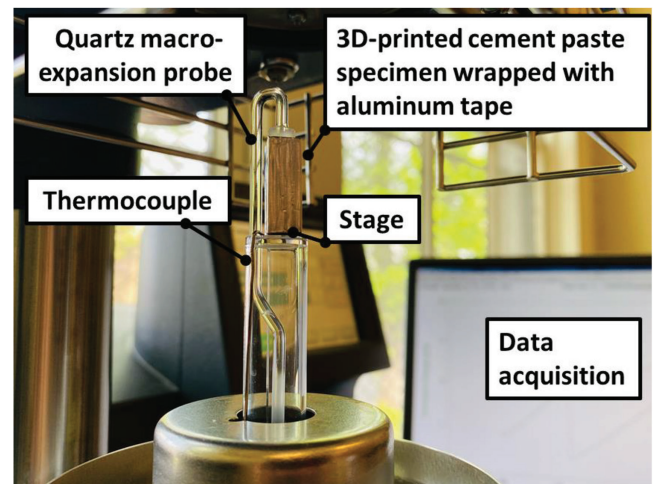


Fig. 2—Representative image of 3-D-printed specimen on glass testing stage of thermomechanical analyzer as it is prepared to be lowered into chamber.

for 91 days in double bags. It is recommended for future studies to keep the specimens at an RH higher than  $93 \pm 2\%$  during the first 24 hours after printing to minimize carbonation and increase hydration.

### Freezing-and-thawing damage quantification using thermomechanical analyzer

Length change measurements were collected using a thermomechanical analyzer.<sup>58,59</sup> After curing, five specimens were cut from each cement paste sample using a high-precision saw with a water-cooled diamond-tipped blade. First, the outer edges of the samples were cut along the dotted lines (Fig. 1(a)). Then, the specimens were cut along the solid lines as illustrated in Fig. 1(a). The dimensions of the cut prismatic specimens were  $7.2 \pm 0.3$  mm wide,  $11.6 \pm 0.3$  mm deep (corresponding to 12 3-D-printed layers), and  $20.3 \pm 0.5$  mm tall. These dimensions were selected to capture several filaments in each specimen and based on the requirements of the TMA stage illustrated in Fig. 2.

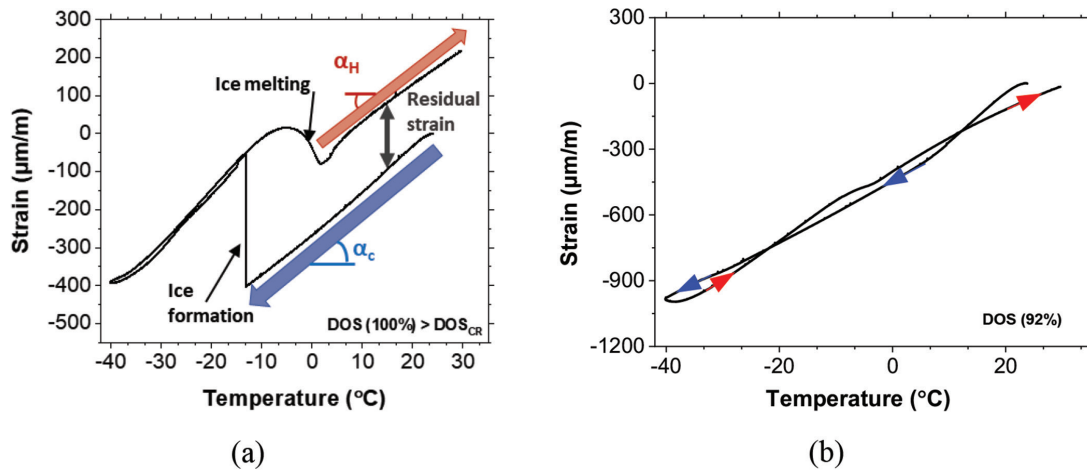


Fig. 3—Strain evolution with respect to temperature in 3-D-printed specimen at: (a) 100% DOS; and (b) 92% DOS.

The 3-D-printed specimens with two different filament orientations (relative to the length change testing direction) and cast specimens were prepared for TMA as follows:

- Prismatic specimens with 3-D-printed filaments and interfaces perpendicular to the direction of the length change measurements (Fig. 1(b)).
- Prismatic specimens with 3-D-printed filaments and interfaces parallel to the direction of length change measurements (Fig. 1(c)).
- Prismatic specimens that do not contain filaments and interfaces that are obtained from the conventional casting of cement paste (Fig. 1(d)).

A comparison between the measurements collected from these three types of specimens was performed to determine the influence of printing and printing directionality on the FT response and the COTE.

For the three geometries illustrated in Fig. 1, specimens with DOS varying from 100 to 91% were prepared to be tested for FT damage using TMA. Upon cutting, the specimens were vacuum saturated according to the procedure described in AASHTO TP 135-20.<sup>63,64</sup> After saturation, the specimens intended to be tested at 100% DOS were taken out of the solution, saturated surface-dried, and their vertical sides were sealed with aluminum tape, as illustrated in Fig. 2, to minimize moisture loss during the test. Immediately thereafter, the specimens were placed in the thermomechanical analyzer for FT damage measurement. The samples prepared to be tested at lower DOS values were left out of the solution at room temperature until reaching the targeted DOS for testing, which was determined by continuously tracking their mass. Immediately after reaching the targeted DOS, the specimens were wrapped in shrink wrap and sealed in double bags at  $23 \pm 1^\circ\text{C}$  for 7 days to allow for an equilibrium of moisture distribution inside the specimen. After 7 days, the specimens were taken out of the bags for a final mass measurement, sealed with aluminum tape on their vertical sides, and placed in the thermomechanical analyzer to measure their FT damage.

Upon mounting the specimen in the TMA chamber, a temperature ramp—cooling from 24 to  $-40^\circ\text{C}$  followed by heating back up to  $30^\circ\text{C}$  at a  $1^\circ\text{C}/\text{min}$  cooling and heating

rate—was applied.<sup>59</sup> The test was performed under a 50 mL/min nitrogen purge rate. A high-precision linear variable differential transformer (LVDT) was used to continuously measure the length change of the specimen. This was done by measuring the movement of the quartz macro-expansion probe that is touching the upper surface of the specimen (Fig. 2).<sup>59</sup> Figure 3(a) illustrates the length change (reported as strain evolution in the longitudinal direction) with respect to temperature obtained from the TMA for a specimen at 100% DOS. During the cooling cycle (from 24 to  $-40^\circ\text{C}$ ), the specimen initially decreases in length as anticipated. However, when ice formation occurs (at approximately  $-14.5 \pm 2.4^\circ\text{C}$ ), there is an increase in the specimen length. The specimen then continues to shrink as the temperature is further reduced. After reaching a temperature of  $-40^\circ\text{C}$  at the initiation of the heating cycle, the specimen is heated and expanded. As the temperature increases, the ice begins to melt, leading to a decrease in specimen length, as observed in Fig. 3(a). After the ice has completely thawed (that is, at approximately  $0.5 \pm 1.9^\circ\text{C}$ ), the specimen continues to expand until the heating cycle is complete (at  $30^\circ\text{C}$ ).

In specimens where the DOS is either below the  $DOS_{CR}$  or close to  $DOS_{CR}$ , the length change of the specimens as they heat and cool follows a similar path, with no ice formation and melting during the cooling and heating (Fig. 3(b)). In contrast, and as illustrated in Fig. 3(a), in DOS higher than  $DOS_{CR}$  where ice forms and FT damage occurs, the specimen will not return to its original length at the end of the first FT cycle. As such, a residual strain remains in the specimen and serves as a direct indication of the FT damage (Fig. 3(a)).<sup>59,65</sup> The COTE during cooling ( $\alpha_c$ ) can be determined by calculating the slope of strain-temperature obtained during cooling and before ice formation (Fig. 3(a)). The COTE during heating ( $\alpha_H$ ) can also be determined by calculating the slope of measurements obtained after ice melting (Fig. 3(a)). While the COTE is generally thought of as linear, a local nonlinearity in the COTE is observed immediately at the end of the ice melting (Fig. 3(a)) and is further discussed later in this paper.

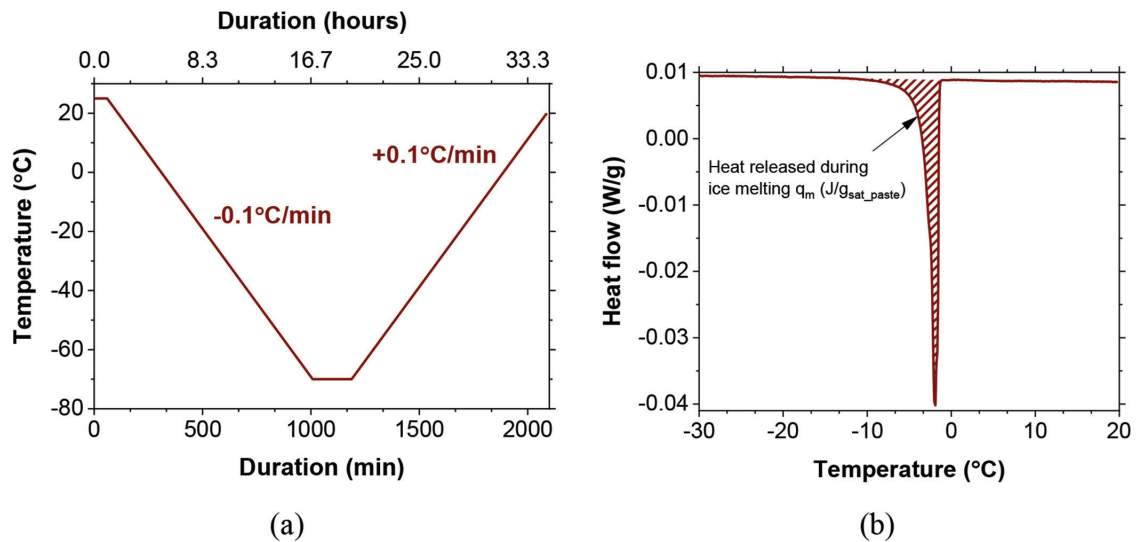


Fig. 4—(a) Temperature ramps during FT cycle in LT-DSC; and (b) ice quantification using heat flow, released during ice melting normalized with respect to gram of saturated cement paste.

### Ice quantification using low-temperature differential scanning calorimetry

The percentage of freezable pore solution was quantified for both the 3-D-printed and cast cement paste specimens with the various DOS ranging from 100 to 75% using a low-temperature differential scanning calorimeter (LT-DSC). Slab-shaped specimens ( $48.5 \pm 2.3$  mg) were extracted from both the 3-D-printed and cast cement paste samples and immersed in saturated lime solution for a duration of  $48 \pm 2$  hours. The slab-shaped specimens contained two interfaces. The slab-shaped specimens were then removed from the lime solution, saturated surface-dried, and sealed in a high-volume platinum pan after reaching the targeted DOS. For the tests that were intended to be performed at 100% DOS, the slab-shaped specimens were sealed immediately inside the pan after being saturated surface-dried, while for lower DOS, the specimens were kept at room temperature until reaching the targeted DOS per continuous mass measurements. The sealed pan was then loaded in the LT-DSC equipment, followed by a cooling ramp from 25 to  $-70^\circ\text{C}$  at a  $0.1^\circ\text{C}/\text{min}$  cooling rate. The specimen was then kept at  $-70^\circ\text{C}$  for 3 hours before following a heating ramp up to  $24^\circ\text{C}$  at  $0.1^\circ\text{C}/\text{min}$  (Fig. 4(a)). The test was performed under a 50 mL/min nitrogen purge rate. The percentage of freezable pore solution that developed in the cement paste was then quantified using Eq. (2)

$$I = \frac{q_m}{q_i} \quad (2)$$

where  $I$  is the gram of ice that was measured per gram of saturated paste ( $g_{ice}/g_{saturated\ paste}$ );  $q_m$  is the heat released during the ice melting per gram of paste ( $J/g_{saturated\ paste}$ ) and was quantified by calculating the area under the peak corresponding to ice melting (Fig. 4(b)); and  $q_i$  is the latent heat of ice equal to  $334 J/g_{ice}$  (that is, the energy required to melt 1 g of ice at  $0^\circ\text{C}$ ).

### Pore-size distribution using dynamic vapor sorption

The influence of the presence of interfaces in the 3-D-printed specimens on the pore-size distribution was determined by comparing the pore-size distribution of the 3-D-printed cement paste specimens with that of the conventionally cast specimens. Slab-shaped specimens ( $110.2 \pm 4.6$  mg) were extracted from both the 3-D-printed cement paste and the cast samples at the end of the curing period. The slab-shaped specimen extracted from the 3-D-printed sample contained three interfaces. The specimens were then vacuum saturated in saturated lime simulated pore solution according to AASHTO TP 135-20.<sup>63</sup> After 48 hours of immersion in the lime simulated pore solution, the slab-shaped specimens were removed from the saturated solution, saturated surface-dried, and placed in a tared quartz pan that was immediately loaded in the environmental chamber of the dynamic vapor sorption (DVS) analyzer to assess the desorption response of the specimens. The specimen mass was continuously monitored during the desorption while the specimens were exposed to the following RH points until the equilibrium point was reached: 97.5, 95, 92.5, 90, 87.5, 85, 82.5, 80, 76, 70, 60, 50, 40, 30, 20, 11, and 0%. The specimens were considered at equilibrium for each RH step when the weight change was less than 0.001% for a duration of 15 minutes or when the RH value was maintained for 98 hours. The measurements were performed at a constant temperature of  $23^\circ\text{C}$  and 10 mL/min nitrogen purge rate.

The pore radius corresponding to each RH step is estimated as the sum of the Kelvin radius, calculated using the Kelvin-Laplace equation<sup>66,67</sup> and the absorbed water film thickness (that is, the  $t$ -curve determined for each RH value).<sup>68-70</sup> The details of the pore-radius calculation can be found in Qiao et al.<sup>71</sup> For each RH, the DOS of the specimens was calculated at equilibrium using Eq. (3)

$$DOS_i = \frac{m_i - m_0}{m_{100} - m_0} \quad (3)$$

where  $DOS_i$  is the DOS of the specimen at each RH step;  $m_0$  is the mass of the specimen at an RH of 0%; and  $m_{100}$  is the saturated surface-dry mass of the specimen at the beginning of the desorption test.

This test quantifies the percentage of capillary pores as well as gel pores for both the 3-D-printed and cast cement paste specimens. This is an important parameter to assess, as based on the Gibbs-Thomson equation, the smaller the pore size, the lower the temperature needed for ice to begin forming.<sup>72</sup> The results obtained from this measurement were correlated with the percentage of freezable pore solution measurements and FT damage measurements.<sup>72</sup>

### Pore characteristics and size distribution using micro-computed tomography

Micro-computed tomography (micro-CT) was used to capture a series of two-dimensional (2-D) X-ray images by rotating the specimen at various angles and reconstructing the images into 2-D slices that can be further analyzed to represent the interior volume of the material.<sup>73,74</sup> The variation in the grayscale intensities assists in the identification of the 3-D spatial distribution of distinct microstructural phases in the specimen.

In this study, an X-ray microscope was used to conduct the microstructural investigations. A wide field of view (FOV) at  $0.4\times$  geometric magnification technique was used to allow for scanning the entire 3-D-printed sample (40 x 50 x 12 mm), which involved the suitable relative positioning of the source, sample, and detector. The  $0.4\times$  magnification corresponded to a resolution of  $36.25\ \mu\text{m}$  (per 1 pixel); thus, the quantification of the percentage of larger capillary pores, with a radius greater than the resolution, present in either the filaments or the interfaces of the 3-D-printed cement paste materials, could be performed. The technique provided a suitable bridge to characterize the capillary pore sizes (in the orders of tens of micrometers) that are not captured by DVS (in the orders of tens of nanometers). The beam energy of 140 keV, power of 10 W, the exposure period of 1 second, and complete 360-degree rotation were employed. The data was post-processed using Avizo 2016<sup>75</sup> to obtain the 3-D reconstructions as well as the 2-D-sliced images.

Binary segmentation of the 2-D slices of the pore and solid phases was conducted by manual thresholding of grayscale intensities using ImageJ software.<sup>76</sup> The binary segmentation was chosen over segmentation with a higher number of phases given the coarse resolutions at  $0.4\times$  magnification. The tangent-slope method was employed to determine the upper threshold intensity limit of pores, which is the intersection point of the tangents at the initial region of the grayscale histogram and the upper region of the hydrated product peak.<sup>77</sup> The binary segmented image was converted to a matrix using MATLAB 2022,<sup>78</sup> where each element corresponded to the grayscale value of each pixel. This matrix is further used to produce the spatial distribution of phases in the 2-D slices.

## RESULTS AND DISCUSSION

### Freezing-and-thawing damage and coefficient of thermal expansion

The length change over the cooling-and-heating cycle, reported as strain evolution with respect to temperature, is illustrated in Fig. 5 for the three types of cement paste specimens tested at 100% DOS. Figures 5(a) and (b) represent the results collected on the 3-D-printed cement paste specimens with the filaments perpendicular and parallel to the longitudinal direction of length change measurements, respectively. Figure 5(c) demonstrates the results obtained on a conventionally cast cement paste specimen with no filaments and interface. The residual strain, as the direct indicator of FT damage,<sup>58,59,65,79</sup> was determined for each of the plots in Fig. 5. In addition, the COTE of the three types of specimens (perpendicular filaments, parallel filaments, and cast specimens without discrete filaments) were determined during both cooling and the heating cycles.

The residual strain measured on the cast cement paste specimen is lower than the values measured on the 3-D-printed cement paste specimens in both the parallel and perpendicular directions (Fig. 5). However, at 100% DOS, this difference between cast specimens and specimens with filaments parallel to the longitudinal direction does not appear to be significant based on the  $t$ -test. At this DOS of 100%, the specimens tested with filaments perpendicular to the longitudinal direction (Fig. 5(a)) showed the highest residual strain value as compared to the other two types of specimens (Fig. 5(b) and (c)), which is in accordance with the findings of Wang et al.<sup>42</sup> This could be due to the fact that FT damage is primarily localized along the weak interfaces, as stated in the literature,<sup>30,34,41</sup> which are perpendicular to the length change measurements for this type of specimen (Fig. 5(a)). However, more data points are required to confirm if the difference observed in residual strain values recorded on specimens with perpendicular filaments direction and the other two types of specimens is significant, and this is due to the inherent statistical variability in the FT response of cementitious materials at full saturation (that is, 100% DOS).<sup>58</sup>

The difference observed between the 3-D-printed and cast values of  $\alpha_C$  and  $\alpha_H$  are insignificant and within the statistical variation (that is, a standard deviation of  $1.3\ \mu\text{m}/(\text{m}\cdot^\circ\text{C})$  and  $0.7\ \mu\text{m}/(\text{m}\cdot^\circ\text{C})$ , respectively). It should be noted that these observations are valid for the specimens tested in this study, with a  $0.275\ \text{w}/\text{c}$  and no printing defects (that is, 20% overlap between filaments<sup>31</sup>). Further work is in progress to investigate the effect of interfacial and layered heterogeneities on the FT response and COTE for specimens with unintentional printing defects (that is, processing parameters that lead to lower overlap or ultimately macroscopic gaps between filaments).

The evolution of the residual strain (that is, FT damage) with respect to the range of DOS (91 to 100%) of specimens for the three types of geometries tested in this study is illustrated in Fig. 6. It can be noted that the  $DOS_{CR}$  for both the cast and 3-D-printed specimens is approximately 91% and appears to be generally independent of the printing directionality. In addition, based on the statistical analysis

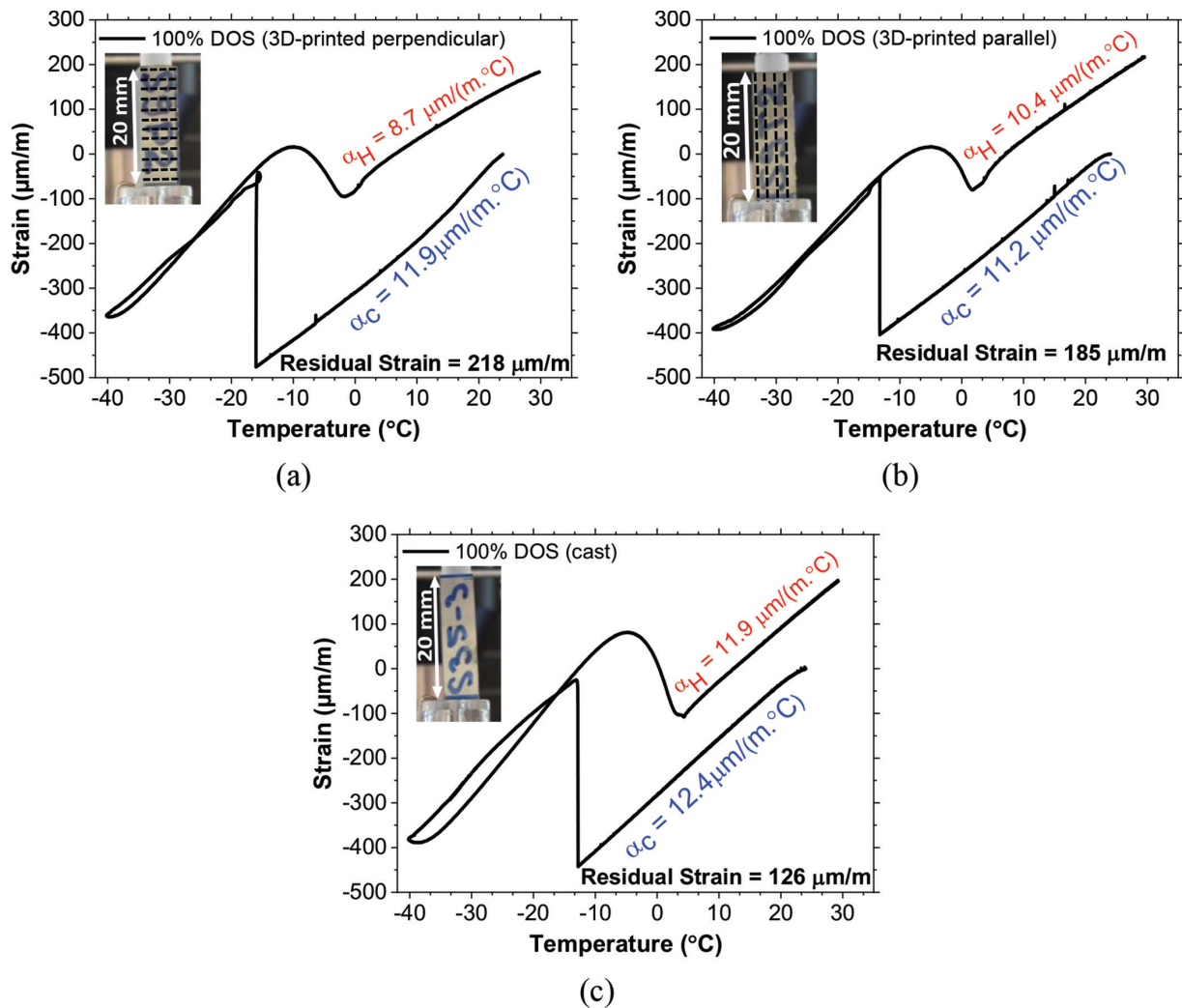


Fig. 5—Strain evolution with respect to temperature for cement paste specimens at 100% DOS with: (a) printed filaments perpendicular to length change measurements; (b) printed filaments parallel to length change measurements; and (c) cast specimen with no filaments.

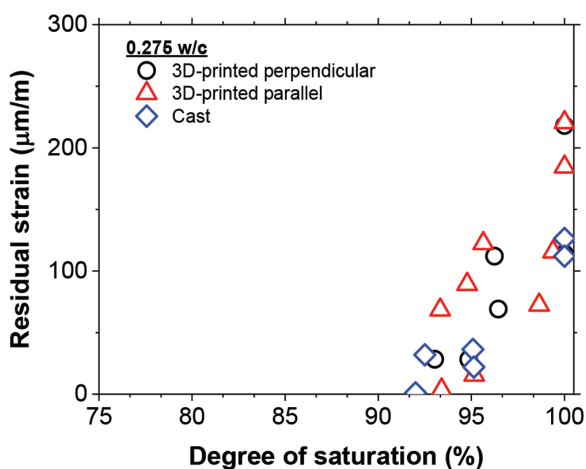


Fig. 6—Residual strain measurements with respect to DOS for three various geometries tested in this study.

of variance (ANOVA) single factor and Tukey test, there is no significant difference in the FT response of the cast and 3-D-printed specimens independent of the printing directionality.

Figures 7(a) and (b) demonstrate the measured COTE ( $\alpha$ ) based on the cooling and heating phases during the TMA test according to the approach illustrated in Fig. 3(a). The linear fitted lines are with an average coefficient of determination,  $R^2$ , of  $0.992 \pm 0.005$  and  $0.995 \pm 0.005$  during cooling and heating, respectively. The observed nonlinearity immediately at the end of the ice melting phase, commented on in Fig. 3(a), is local and does not significantly influence the  $R^2$  values of the linear fitted lines. It can be noted that both  $\alpha_C$  and  $\alpha_H$  increase with the decrease in the DOS for both the cast and 3-D-printed cement paste specimens. The COTE of all the specimens tested in this study fall within the range of values measured on mature cement paste in the literature (that is, range between  $8 \times 10^{-6} \text{C}^{-1}$  and  $22 \times 10^{-6} \text{C}^{-1}$ ).<sup>80-85</sup> No significant difference can be noted between the COTE values measured on the cast specimens as compared to the printed specimens independent of the printing directionality.

Based on the results of Fig. 6 and 7, it can be concluded that for this mixture design (0.275 w/c), and for specimens with no printing defects (that is, 20% overlap between filaments<sup>31</sup>), the printing directionality does not influence the  $DOS_{CR}$  of these specimens or FT response at DOS below

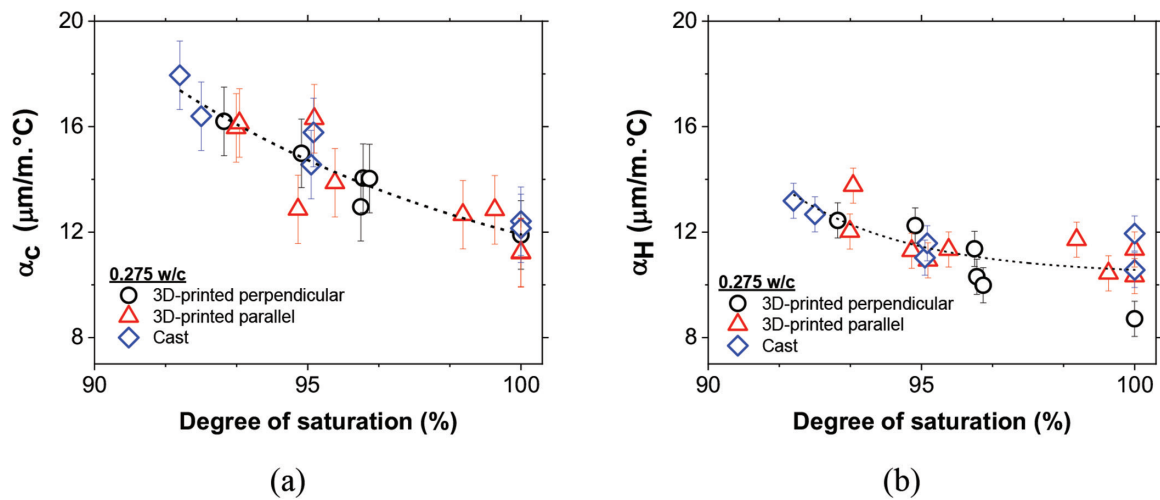


Fig. 7—Coefficient of thermal contraction and expansion from cooling-and-heating cycles of TMA test, plotted with respect to DOS for three types of geometries under: (a) contraction; and (b) expansion.

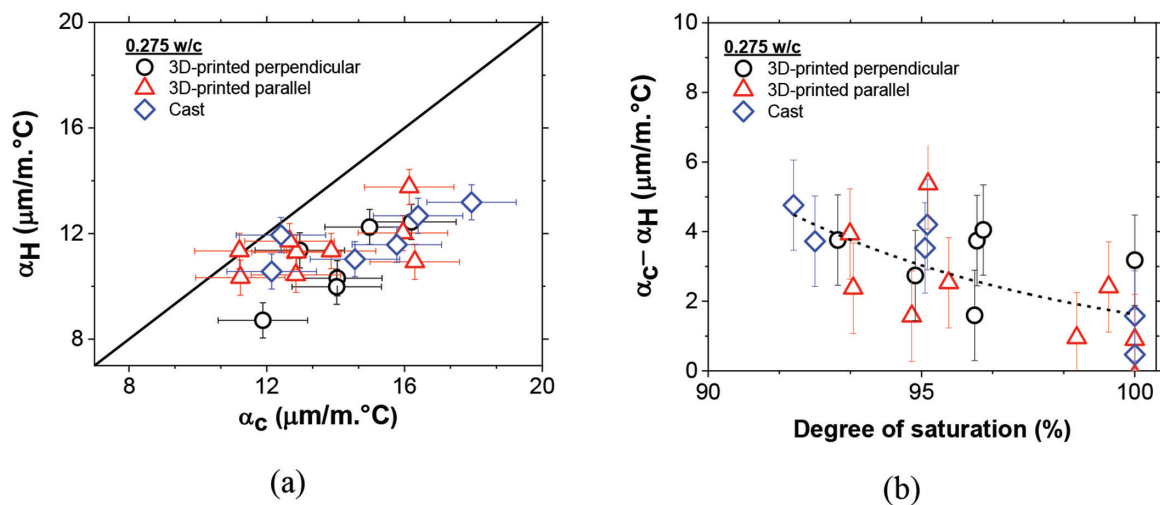


Fig. 8—(a) Coefficient of thermal expansion of 3-D-printed and cast cement paste specimens during heating compared to coefficient of thermal expansion during cooling; and (b) comparison of difference between coefficients of thermal expansion during cooling and heating with respect to DOS.

100%. As such, well-printed specimens have isotropic COTE and  $DOS_{CR}$  values. Ongoing work is underway examining the influence of printing defects by varying filament overlap. 3-D-printed samples with 100% DOS appear to have a higher FT damage as compared to their cast counterpart samples; however, due to the inherent variability in the FT damage at 100% DOS, additional data points are needed to confirm if this observed difference is statistically significant.

For all specimens,  $\alpha_H$  values are either similar to or lower than  $\alpha_C$ , as illustrated in Fig. 8(a), and the difference between  $\alpha_H$  and  $\alpha_C$  increases with the decrease in the DOS of the specimen (Fig. 8(b)).

A typical nonlinearity in the strain evolution response was observed, immediately at the end of the ice melting phase and before the linear temperature up-ramp (Fig. 9(a)). To more clearly illustrate this, Fig. 9(b) illustrates the derivative of the strain evolution (that is, the COTE) with respect to the temperature during the entire cooling-and-heating cycle. The derivative of the strain evolution with temperature highlights

the ice formation point (Fig. 9(c)), ice melting, and nonlinear after-melting points (Fig. 9(d)). This nonlinear response at the end of the ice melting phase, magnified in Fig. 9(d), can be explained by the redistribution of water inside the pores of the cementitious matrix.<sup>86,87</sup> During the cooling phase, water moves from the smaller to larger pores.<sup>86,87</sup> During the heating phase, water moves from larger to smaller pores,<sup>86</sup> explaining differences between  $\alpha_H$  and  $\alpha_C$  ( $\alpha_H$  being lower than  $\alpha_C$ , as shown in Fig. 8(a)).

In this study, for specimens at full saturation (100% in this study), cracks can form due to FT damage, which would decrease the COTE<sup>88</sup> (that is, during the heating cycle). This explains the decrease in the difference between  $\alpha_C$  and  $\alpha_H$  with the increase in DOS (that is, an increase in FT damage) (Fig. 8(b)).

### Influence of interface on ice formation and pore-size distribution

Figure 10 illustrates the percentage of freezable pore solution (obtained from LT-DSC) with respect to the DOS of both

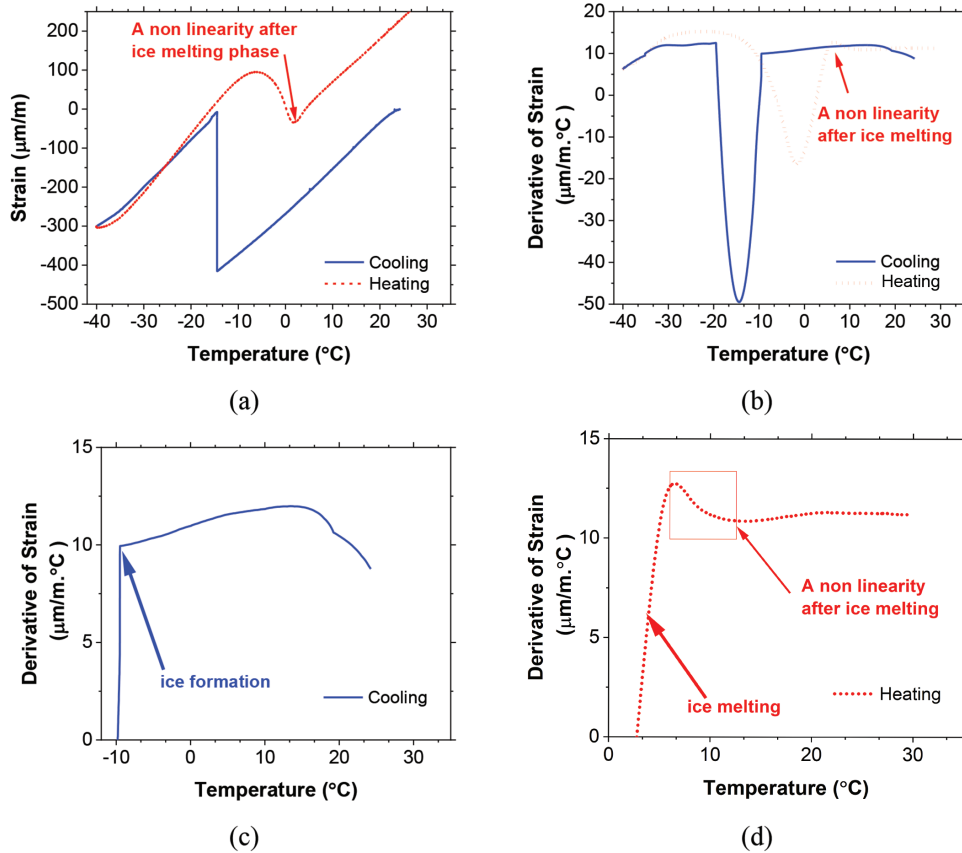


Fig. 9—(a) Strain evolution with respect to temperature (100% DOS); and derivative of strain with respect to temperature: (b) for entire FT cycle; (c) before ice formation; and (d) after ice melting.

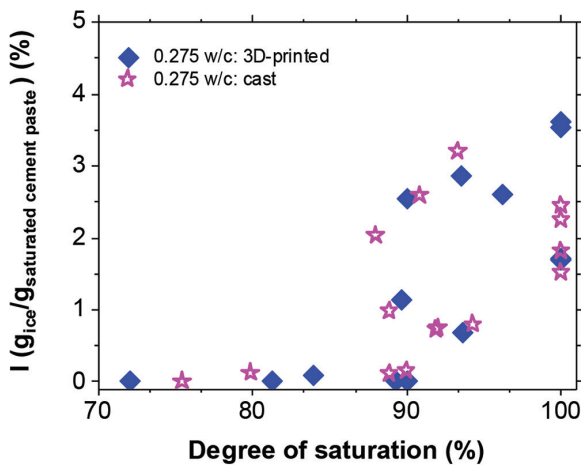


Fig. 10—Percentage of freezable pore solution with respect to DOS.

the 3-D-printed and cast cement paste specimens with a  $w/c$  of 0.275. It can be noted based on Fig. 10 that the percentage of freezable pore solution in the 3-D-printed and cast specimens is closely comparable. The statistical ANOVA single factor and Tukey test confirmed that there is no significant difference between these two data sets. In addition, the percentage of freezable pore solution decreases with the decrease in the DOS in all specimen types, as expected. This is in accordance with the correlation observed between the DOS and the residual strain values (that is, FT damage), as illustrated in Fig. 6.

Pores with a pore radius greater than 5 nm correspond to large pores such as capillary pores, air voids, and directional interfacial pores in the case of 3-D-printed samples. Pores with a pore radius below 5 nm can be filled with gel water, surface water, and phase water.<sup>89</sup> Water in capillary pores can freeze during an FT cycle, while only a portion of gel pores solution is able to freeze.<sup>90,91</sup> The desorption curves and pore-size distribution curves measured in this study for both the 3-D-printed cement paste and cast specimens are illustrated in Fig. 11(a) and (b), respectively. A coarser pore structure is measured for the 3-D-printed cement paste specimens, which may be related to the interface porosity. For the cast cement paste specimens, only 13% of the pores have a pore radius above 5 nm, and this percentage explains the low percentage of freezable pore solution in Fig. 10. The 3-D-printed specimens showed a higher percentage of coarser pores ( $>5$  nm), equal to 28% of the pores (Fig. 11). However, the total porosity of the samples tested in this study with a  $w/c$  of 0.275 is low (that is,  $\sim 27\%$  of the specimen volume obtained from Powers' model<sup>48</sup>).

In summary, using a low  $w/c$  in the mixture design of 3-D-printed cement paste may be beneficial for increasing the FT resistance of the materials by decreasing the percentage of freezable pore solution.

### Influence of interfacial heterogeneity of 3-D-printed materials on FT response

Reconstructions of the 3-D-printed cement paste specimens and the representative 2-D slices in two different

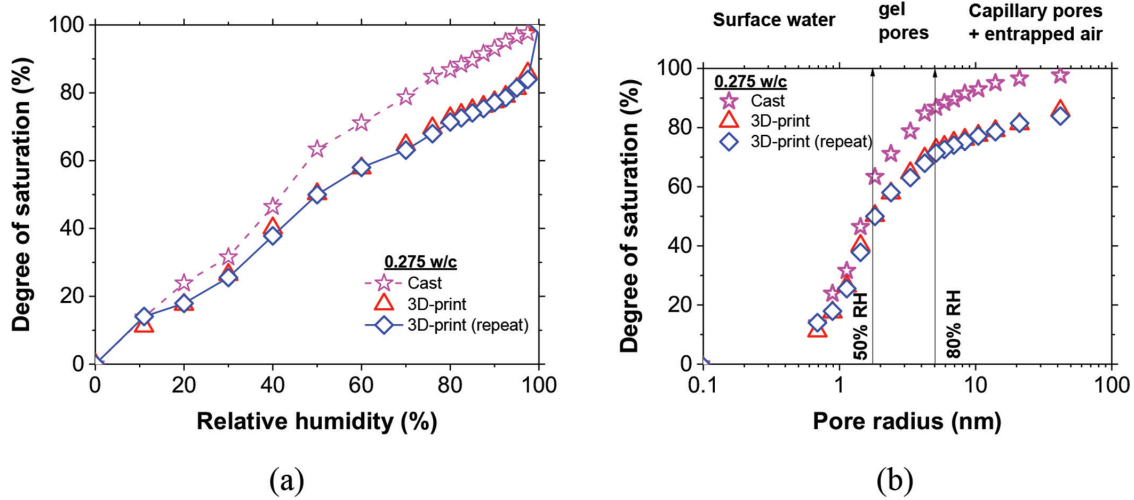


Fig. 11—(a) Sorption isotherm collected on 3-D-printed and conventionally cast cement paste specimens; and (b) pore-size distribution of 3-D-printed and conventionally cast cement paste specimens.

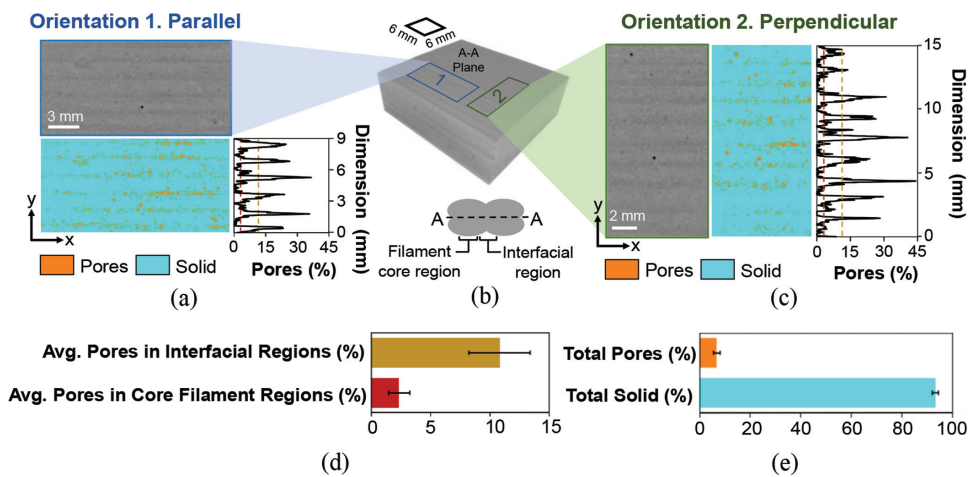


Fig. 12—(a) 2-D-micro-CT raw and segmented images in parallel direction; (b) 3-D-micro-CT rendering of additively manufactured cement paste; (c) 2-D-micro-CT raw and segmented images in perpendicular direction; (d) comparison of pore phase in interfacial region and core filament region; and (e) percentages of total pore and solid phases in 3-D-printed materials.

orientations along with their binary segmented images are presented in Fig. 12(a) to (c). The 2-D slices of the specimen in the parallel (orientation 1) and perpendicular (orientation 2) are shown in Fig. 12(b) in rectangular boxes and illustrated in Fig. 12(a) and (c), respectively. These raw 2-D slices are obtained from the horizontal interface between the two 3-D-printed layers, as presented in Plane A-A in Fig. 12(b). In the raw 2-D slices in both orientations, the pore phase is demonstrated by the darker gray regions, and the solid phase (that is, hydrated and unhydrated cement) is represented as brighter gray regions. These darker regions qualitatively illustrate the presence of pores at the filament interfaces, highlighting the concentration of pores surrounding the filaments (that is, interfacial regions around the filament cores). Using binary segmentation, the 2-D distribution of the pore phase versus the solid phase is plotted in Fig. 12(a) and (c) to quantitatively capture the heterogeneous characteristics of 3-D-printed materials. In these segmented images, the pore phase and solid phases are represented by the orange and cyan colors, respectively. The cumulative distribution of the pore phase as the phase of interest is shown along

the x-direction as a function of distance from the bottom of the segmented images in the y-direction. (Fig. 12(a) and (c)) The amount of porosity in the 2-D-sliced images alters quite significantly from as high as 45% in the interfacial regions to as low as 0.2% in the core filament regions. This is a frequent heterogeneity that is commensurate with the qualitative observations of the frequency of darker regions in the raw sliced images. This spatial variation in the pore heterogeneity was found to be nearly uniform given the pore peaks were located at a relatively constant spacing of 1.64 mm (ranging from 1.56 to 1.7 mm) corresponding to the nominal filament width used in slicing (1.63 mm). This pore peak spacing associated with the (cumulative) porosity at the interfacial regions corroborates well with the pore plateau spacing of the (cumulative) porosity associated with the core filament regions.

To better capture the microstructural heterogeneity, the average pore phase in the interfacial region versus the core filament region is quantified and plotted in Fig. 12(d). The values plotted in Fig. 12(d) are also shown as brown and red dashed lines in Fig. 12(a) and (c). The interfacial and filament

core regions of equal width (along the y-axis) were assumed based on the cumulative distribution of porosity along the 2-D-sliced images, with the peaks in the pore distribution plots taken as the center of the interfacial region. Using the moving averages of the data in Fig. 12(a) and (c), it was observed that the average porosity in the interfacial region is 10.8% compared to the 2.3% average porosity at the filament core regions. The 4.6 times higher average interfacial porosity additionally indicated significant heterogeneity in the bulk-layered microstructure of the 3-D-printed cement paste materials. Such a significant heterogeneity in the pore microstructure of the 3-D-printed materials is exacerbated by the underlying nonuniform distributions observed in Fig. 12(a) and (c) and can directly impact the characteristics of FT response compared to the cast counterparts with a homogeneous microstructure. This finding confirms that the coarser pore-size distribution in the 3-D-printed specimens observed using the DVS at the nanoscale is related to the interfacial porosity.

The total porosity based on the 2-D-sliced images is characterized and presented in Fig. 12(e). The total bulk pore phase was quantified as 6.7%, which closely corresponds to 6.6% as the mean of the two average data points for the interfacial and core filament regions presented in Fig. 12(d). It should be noted that the resolution of the  $0.4\times$  magnification limits the size of quantifiable pores at  $36.25\ \mu\text{m}$ , and imaging at higher magnification is a subject of ongoing research to better capture the smaller spatial pore distribution.

## CONCLUSIONS

This paper examined the influence of the printing directionality on the freezing-and-thawing (FT) response, critical degree of saturation ( $DOS_{CR}$ ), and coefficient of thermal expansion (COTE) of three-dimensional (3-D)-printed cement paste specimens with various degrees of saturation (DOS) in comparison with conventionally cast specimens. The FT response measurements were performed using thermomechanical analysis (TMA) on a mixture design with a water-cement ratio ( $w/c$ ) of 0.275. The pore microstructure was characterized by using micro-computed tomography (micro-CT).

For the mixtures tested (0.275  $w/c$ ), the  $DOS_{CR}$ , COTE, and FT response of the 3-D-printed cement paste specimen with a DOS less than 100% were independent of the printing directionality and were comparable to the conventionally cast cement paste. The  $DOS_{CR}$  was approximately 91% for all specimens tested, which is at the upper end of various types of conventional concrete.

The COTE of both the 3-D-printed and cast cement paste specimens increased with a decrease in the DOS from 100 to 91%. The COTE values measured during the heating phase of the specimens were lower than the values measured during the cooling. This is likely caused by the redistribution of water inside the pores.

The 3-D-printed specimens with a 100% DOS appear to have higher FT damage as compared to the cast specimens. The 3-D-printed specimens with perpendicular filaments showed the greatest FT damage at 100% DOS as compared to the other two types of specimens (that is, filaments in the

parallel direction and cast specimens). However, due to the inherent variability in the FT damage at 100% DOS, additional data points are needed to confirm if this observed difference is statistically significant.

The percentage of freezable pore solution with respect to the DOS was measured to be comparable for both the cast and 3-D-printed cement paste specimens. This percentage of freezable pore solution was small ( $\sim 4g_{ice}/100g_{paste}$  at 100% DOS), mainly due to the low  $w/c$  of the mixture design. Consequently, the low  $w/c$  in the mixture designs of the 3-D-printed cement paste can be beneficial in increasing the FT resistance due to a reduction in the capillary porosity and the percentage of freezable pore solution.

The 3-D-printed specimens showed a coarser pore-size distribution as compared to conventionally cast specimens (mainly due to the presence of interfacial porosity).

The micro-CT analysis demonstrated that the amount of porosity in the two-dimensional (2-D)-sliced images significantly alters from 45% in the interfacial regions to 0.2% in the core filament regions, with a nonuniform pore distribution but a rather uniform filament spacing in each region. This is a frequent heterogeneity in 3-D-printed material and is commensurate with the observations of the frequency of darker interfacial regions in the raw sliced images. Such a significant heterogeneity in the pore microstructure of 3-D-printed materials can directly impact their FT response. The uniform spatial variation of the pore phase was found at a relatively constant frequency of 1.64 mm corresponding to the nominal filament width used in slicing. Moving averages indicated that the mean porosity in the interfacial region is 10.8% compared to the 2.3% average porosity at the filament core regions. The 4.6 times higher average interfacial porosity additionally supports the significant heterogeneity in the bulk-layered microstructure of 3-D-printed cement paste materials.

In conclusion, 3-D-printed cement paste specimens with a low  $w/c$  (0.275) and no visible printing defects (20% overlapping between printed filaments) have a similar  $DOS_{CR}$  to conventionally cast specimens. The performance of the 3-D-printed specimen was independent of the printing directionality for DOS below 100%. However, the anisotropy in the FT performance of the layered fabrication process and printing-induced interfaces and defects is an area of ongoing study. In addition, the influence of filament porosity on the rate of water absorption is still being studied.

## AUTHOR BIOS

**Rita Maria Ghantous** is a Research Associate in the School of Civil and Construction Engineering at Oregon State University, Corvallis, OR. She received her MS from the École Centrale de Nantes, Nantes, France, and her PhD in civil engineering from the Institut National des Sciences Appliquées (INSA) Toulouse, Toulouse, France. Her research interests include carbonation, durability, and sustainability of concrete and cementitious materials.

**Anastasiia Evseeva** is an Undergraduate Research Assistant in the School of Civil and Construction Engineering at Oregon State University.

**Brandon Dickey** is an Undergraduate Research Assistant majoring in business administration in international business. His research interests include three-dimensional (3-D) construction printing and sustainable communities.

ACI member **Shashank Gupta** is a PhD Student in the Department of Civil and Environmental Engineering at Princeton University, Princeton, NJ. He received his BE (Hons) in civil engineering from the Birla Institute of Technology & Science (BITS) Pilani, Pilani, Rajasthan, India, and his MSc in civil engineering from Politecnico di Milano, Milan, Italy.

ACI member **Arjun Prihar** is an MSE Student in the Department of Civil and Environmental Engineering at Princeton University. He received his BSc in civil engineering from The University of British Columbia, Vancouver, BC, Canada.

**Hadi Shagerdi Esmaeeli** is an Associate Research Scholar in the Department of Civil and Environmental Engineering at Princeton University. He received his BSc in civil engineering from the University of Tabriz, Tabriz, Iran, and his MSc and PhD in civil engineering from Purdue University, West Lafayette, IN. He is a member of ACI Committees 201, Durability of Concrete; 236, Material Science of Concrete; and 564, 3-D Printing with Cementitious Materials. His research interests include additive manufacturing and computational mechanics toward developing resilient infrastructure.

ACI member **Reza Moini** is an Assistant Professor of civil and environmental engineering at Princeton University. He received his BSc from Qom University, Qom, Iran, and his MSc from the University of Wisconsin-Milwaukee, Milwaukee, WI, both in civil and environmental engineering, and his PhD from Purdue University Lyles School of Civil Engineering. He is Secretary of ACI Subcommittee 211-M, Aggregate Packing Model, and a member of ACI Committee 564, 3-D Printing with Cementitious Materials. His research interests include the mechanics of resilient and multifunctional architected materials enabled by automated and robotic manufacturing techniques.

**W. Jason Weiss**, FACI, is the Edwards Distinguished Chair at Oregon State University. He received his BAE from The Pennsylvania State University, University Park, PA, and his MS and PhD from Northwestern University, Evanston, IL, in 1995, 1997, and 1999, respectively. He is Editor-in-Chief of the ACI Materials Journal, and a member of the ACI Technical Activities Committee (TAC).

## ACKNOWLEDGMENTS

The authors gratefully acknowledge support for this work from the National Science Foundation (Award Numbers 2129566 and 2129606) and the U.S. Endowment. The authors are grateful to the MBCC Group and Buzzi Unicem for providing materials for this research work.

## REFERENCES

- Gosselin, C.; Duballet, R.; Roux, P.; Gaudillière, N.; Dirrenberger, J.; and Morel, P., "Large-Scale 3D Printing of Ultra-High Performance Concrete – A New Processing Route for Architects and Builders," *Materials & Design*, V. 100, June 2016, pp. 102-109. doi: 10.1016/j.matdes.2016.03.097
- Buswell, R. A.; Soar, R. C.; Gibb, A. G. F.; and Thorpe, A., "Freeform Construction: Mega-Scale Rapid Manufacturing for Construction," *Automation in Construction*, V. 16, No. 2, Mar. 2007, pp. 224-231. doi: 10.1016/j.autcon.2006.05.002
- Buswell, R. A.; Leal de Silva, W. R.; Jones, S. Z.; and Dirrenberger, J., "3D Printing Using Concrete Extrusion: A Roadmap for Research," *Cement and Concrete Research*, V. 112, Oct. 2018, pp. 37-49. doi: 10.1016/j.cemconres.2018.05.006
- Khoshnevis, B., "Automated Construction by Contour Crafting—Related Robotics and Information Technologies," *Automation in Construction*, V. 13, No. 1, Jan. 2004, pp. 5-19. doi: 10.1016/j.autcon.2003.08.012
- Delgado Camacho, D.; Clayton, P.; O'Brien, W. J.; Seepersad, C.; Juenger, M.; Ferron, R.; and Salamone, S., "Applications of Additive Manufacturing in the Construction Industry – A Forward-Looking Review," *Automation in Construction*, V. 89, May 2018, pp. 110-119. doi: 10.1016/j.autcon.2017.12.031
- Mechtcherine, V.; Bos, F. P.; Perrot, A.; Leal da Silva, W. R.; Nerella, V. N.; Fataei, S.; Wolfs, R. J. M.; Sonebi, M.; and Roussel, N., "Extrusion-Based Additive Manufacturing with Cement-Based Materials – Production Steps, Processes, and Their Underlying Physics: A Review," *Cement and Concrete Research*, V. 132, June 2020, Article No. 106037.
- Khan, M. S.; Sanchez, F.; and Zhou, H., "3-D Printing of Concrete: Beyond Horizons," *Cement and Concrete Research*, V. 133, July 2020, Article No. 106070.
- Wangler, T.; Lloret, E.; Reiter, L.; Hack, N.; Gramazio, F.; Kohler, M.; Bernhard, M.; Dillenburger, B.; Buchli, J.; Roussel, N.; and Flatt, R.,

"Digital Concrete: Opportunities and Challenges," *RILEM Technical Letters*, V. 1, 2016, pp. 67-75. doi: 10.21809/rilemtechlett.2016.16

9. Biernacki, J. J.; Bullard, J. W.; Sant, G.; Brown, K.; Glasser, F. P.; Jones, S.; Ley, T.; Livingston, R.; Nicoleau, L.; Olek, J.; Sanchez, F.; Shahsavari, R.; Stutzman, P. E.; Sobolev, K.; and Prater, T., "Cements in the 21st Century: Challenges, Perspectives, and Opportunities," *Journal of the American Ceramic Society*, V. 100, No. 7, July 2017, pp. 2746-2773. doi: 10.1111/jace.14948

10. Barbosa, F.; Woetzel, J.; Mischke, J.; João Ribeirinho, M.; Sridhar, M.; Parsons, M.; Bertram, N.; and Brown, S., "Reinventing Construction: A Route to Higher Productivity," McKinsey Global Institute, 2017, 168 pp.

11. Schultdt, S. J.; Jagoda, J. A.; Hoisington, A. J.; and Delorit, J. D., "A Systematic Review and Analysis of the Viability of 3D-Printed Construction in Remote Environments," *Automation in Construction*, V. 125, May 2021, Article No. 103642.

12. Allouzi, R.; Al-Azhari, W.; and Allouzi, R., "Conventional Construction and 3D Printing: A Comparison Study on Material Cost in Jordan," *Journal of Engineering*, V. 2020, 2020, Article No. 1424682.

13. De Schutter, G.; Lesage, K.; Mechtcherine, V.; Nerella, V. N.; Habert, G.; and Agusti-Juan, I., "Vision of 3D Printing with Concrete—Technical, Economic and Environmental Potentials," *Cement and Concrete Research*, V. 112, Oct. 2018, pp. 25-36. doi: 10.1016/j.cemconres.2018.06.001

14. Moini, R.; Olek, J.; Youngblood, J. P.; Magee, B.; and Zavattieri, P. D., "Additive Manufacturing and Performance of Architected Cement-Based Materials," *Advanced Materials*, V. 30, No. 43, Oct. 2018, Article No. 1802123.

15. Marchon, D.; Kawashima, S.; Bessaies-Bey, H.; Mantellato, S.; and Ng, S., "Hydration and Rheology Control of Concrete for Digital Fabrication: Potential Admixtures and Cement Chemistry," *Cement and Concrete Research*, V. 112, Oct. 2018, pp. 96-110. doi: 10.1016/j.cemconres.2018.05.014

16. Roussel, N., "Rheological Requirements for Printable Concretes," *Cement and Concrete Research*, V. 112, Oct. 2018, pp. 76-85. doi: 10.1016/j.cemconres.2018.04.005

17. Ma, G., and Wang, L., "A Critical Review of Preparation Design and Workability Measurement of Concrete Material for Largescale 3D Printing," *Frontiers of Structural and Civil Engineering*, V. 12, No. 3, Sept. 2018, pp. 382-400. doi: 10.1007/s11709-017-0430-x

18. Kazemian, A.; Yuan, X.; Cochran, E.; and Khoshnevis, B., "Cementitious Materials for Construction-Scale 3D Printing: Laboratory Testing of Fresh Printing Mixture," *Construction and Building Materials*, V. 145, Aug. 2017, pp. 639-647. doi: 10.1016/j.conbuildmat.2017.04.015

19. Tay, Y. W.; Panda, B.; Paul, S. C.; Tan, M. J.; Qian, S. Z.; Leong, K. F.; and Chua, C. K., "Processing and Properties of Construction Materials for 3D Printing," *Materials Science Forum*, V. 861, 2016, pp. 177-181. doi: 10.4028/www.scientific.net/MSF.861.177

20. Rodriguez, F. B.; Olek, J.; Moini, R.; Zavattieri, P. D.; and Youngblood, J. P., "Linking Solids Content and Flow Properties of Mortars to Their Three-Dimensional Printing Characteristics," *ACI Materials Journal*, V. 118, No. 6, Nov. 2021, pp. 371-382.

21. Moini, R.; Olek, J.; Zavattieri, P. D.; and Youngblood, J. P., "Open-Span Printing Method for Assessment of Early-Age Deformations of Additively Manufactured Cement-Based Materials Using an Isosceles Triangle," *ASTM Symposium on Standards Development for Cement and Concrete Used in Additive Construction*, S. Z. Jones and E. L. Kreiger, eds., 2021, pp. 1-12.

22. Sanjayam, J. G.; Nematollahi, B.; Xia, M.; and Marchment, T., "Effect of Surface Moisture on Inter-Layer Strength of 3D Printed Concrete," *Construction and Building Materials*, V. 172, May 2018, pp. 468-475. doi: 10.1016/j.conbuildmat.2018.03.232

23. Tay, Y. W. D.; Ting, G. H. A.; Qian, Y.; Panda, B.; He, L.; and Tan, M. J., "Time Gap Effect on Bond Strength of 3D-Printed Concrete," *Virtual and Physical Prototyping*, V. 14, No. 1, 2019, pp. 104-113. doi: 10.1080/17452759.2018.1500420

24. Van Der Putten, J.; De Schutter, G.; and Van Tittelboom, K., "The Effect of Print Parameters on the (Micro)structure of 3D Printed Cementitious Materials," *First RILEM International Conference on Concrete and Digital Fabrication – Digital Concrete 2018*, T. Wangler and R. J. Flatt, eds., Zurich, Switzerland, Springer, Cham, Switzerland, 2019, pp. 234-244.

25. Moini, R.; Baghaie, A.; Rodriguez, F. B.; Zavattieri, P. D.; Youngblood, J. P.; and Olek, J., "Quantitative Microstructural Investigation of 3D-Printed and Cast Cement Pastes Using Micro-Computed Tomography and Image Analysis," *Cement and Concrete Research*, V. 147, Sept. 2021, Article No. 106493.

26. Wolfs, R. J. M.; Bos, F. P.; and Salet, T. A. M., "Hardened Properties of 3D Printed Concrete: The Influence of Process Parameters on Interlayer Adhesion," *Cement and Concrete Research*, V. 119, May 2019, pp. 132-140. doi: 10.1016/j.cemconres.2019.02.017

27. Wangler, T.; Aguilar Sanchez, A. M.; Anton, A.; Dillenburger, B.; and Flatt, R. J., "Two Year Exposure of 3D Printed Cementitious Columns in a High Alpine Environment," *Third RILEM International Conference on Concrete and Digital Fabrication: Digital Concrete 2022*, R. Buswell, A. Blanco, S. Cavalaro, and P. Kinnell, eds., Loughborough, UK, Springer, Cham, Switzerland, 2022, pp. 182-187.
28. Mohan, M. K.; Rahul, A. V.; De Schutter, G.; and Van Tittelboom, K., "Salt Scaling Resistance of 3D Printed Concrete," *Third RILEM International Conference on Concrete and Digital Fabrication: Digital Concrete 2022*, R. Buswell, A. Blanco, S. Cavalaro, and P. Kinnell, eds., Loughborough, UK, Springer, Cham, Switzerland, 2022, pp. 188-193.
29. Aguilar Sanchez, A. M.; Wangler, T.; Stefanoni, M.; and Angst, U., "Microstructural Examination of Carbonated 3D-Printed Concrete," *Journal of Microscopy*, V. 286, No. 2, May 2022, pp. 141-147. doi: 10.1111/jmi.13087
30. Das, A.; Aguilar Sanchez, A. M.; Wangler, T.; and Flatt, R. J., "Freeze-Thaw Performance of 3D Printed Concrete: Influence of Interfaces," *Third RILEM International Conference on Concrete and Digital Fabrication: Digital Concrete 2022*, R. Buswell, A. Blanco, S. Cavalaro, and P. Kinnell, eds., Loughborough, UK, Springer, Cham, Switzerland, 2022, pp. 200-205.
31. Rodriguez, F. B.; Garzon Lopez, C.; Wang, Y.; Olek, J.; Zavattieri, P. D.; Youngblood, J. P.; Falzone, G.; and Cotrell, J., "Evaluation of Durability of 3D-Printed Cementitious Materials for Potential Applications in Structures Exposed to Marine Environments," *Third RILEM International Conference on Concrete and Digital Fabrication: Digital Concrete 2022*, R. Buswell, A. Blanco, S. Cavalaro, and P. Kinnell, eds., Loughborough, UK, Springer, Cham, Switzerland, 2022, pp. 175-181.
32. Schröfl, C.; Nerella, V. N.; and Mechtcherine, V., "Capillary Water Intake by 3D-Printed Concrete Visualised and Quantified by Neutron Radiography," *First RILEM International Conference on Concrete and Digital Fabrication – Digital Concrete 2018*, T. Wangler and R. J. Flatt, eds., Zurich, Switzerland, Springer, Cham, Switzerland, 2019, pp. 217-224.
33. Van Der Putten, J.; De Smet, M.; Van den Heede, P.; De Schutter, G.; and Van Tittelboom, K., "Influence of the Print Process on the Durability of Printed Cementitious Materials," *Third RILEM International Conference on Concrete and Digital Fabrication: Digital Concrete 2022*, R. Buswell, A. Blanco, S. Cavalaro, and P. Kinnell, eds., Loughborough, UK, Springer, Cham, Switzerland, 2022, pp. 194-199.
34. Zhang, Y.; Zhang, Y.; Yang, L.; Liu, G.; Chen, Y.; Yu, S.; and Du, H., "Hardened Properties and Durability of Large-Scale 3D Printed Cement-Based Materials," *Materials and Structures*, V. 54, No. 1, Feb. 2021, Article No. 45. doi: 10.1617/s11527-021-01632-x
35. Das, A.; Song, Y.; Mantellato, S.; Wangler, T.; Lange, D. A.; and Flatt, R. J., "Effect of Processing on the Air Void System of 3D Printed Concrete," *Cement and Concrete Research*, V. 156, June 2022, Article No. 106789.
36. Moini, M.; Olek, J.; Magee, B.; Zavattieri, P.; and Youngblood, J., "Additive Manufacturing and Characterization of Architected Cement-Based Materials via X-Ray Micro-computed Tomography," *First RILEM International Conference on Concrete and Digital Fabrication – Digital Concrete 2018*, T. Wangler and R. J. Flatt, eds., Zurich, Switzerland, Springer, Cham, Switzerland, 2019, pp. 176-189.
37. Powers, T. C., and Willis, T. F., "The Air Requirement of Frost Resistant Concrete," *Highway Research Board Proceedings*, V. 29, 1950, pp. 184-211.
38. Smith, S. H.; Kurtis, K. E.; and Tien, I., "Probabilistic Evaluation of Concrete Freeze-Thaw Design Guidance," *Materials and Structures*, V. 51, No. 5, Oct. 2018, Article No. 124. doi: 10.1617/s11527-018-1259-z
39. Du, L., and Folliard, K. J., "Mechanisms of Air Entrainment in Concrete," *Cement and Concrete Research*, V. 35, No. 8, Aug. 2005, pp. 1463-1471. doi: 10.1016/j.cemconres.2004.07.026
40. Tunstall, L. E.; Scherer, G. W.; and Prud'homme, R. K., "Studying AEA Interaction in Cement Systems Using Tensiometry," *Cement and Concrete Research*, V. 92, Feb. 2017, pp. 29-36. doi: 10.1016/j.cemconres.2016.11.005
41. Assaad, J. J.; Hamzeh, F.; and Hamad, B., "Qualitative Assessment of Interfacial Bonding in 3D Printing Concrete Exposed to Frost Attack," *Case Studies in Construction Materials*, V. 13, Dec. 2020, Article No. e00357.
42. Wang, L.; Xiao, W.; Wang, Q.; Jiang, H.; and Ma, G., "Freeze-Thaw Resistance of 3D-Printed Composites with Desert Sand," *Cement and Concrete Composites*, V. 133, Oct. 2022, Article No. 104693. doi: 10.1016/j.cemconcomp.2022.104693
43. Fagerlund, G., "The Critical Degree of Saturation Method of Assessing the Freeze/Thaw Resistance of Concrete," *Matériaux et Constructions*, V. 10, No. 4, July 1977, pp. 217-229.
44. Fagerlund, G., "A Service Life Model for Internal Frost Damage in Concrete," Report TVBM, V. 3119, Division of Building Materials, LTH, Lund University, Lund, Sweden, 2004, 138 pp.
45. Todak, H.; Lucero, C.; and Weiss, W. J., "Why Is the Air There? Thinking about Freeze-Thaw in Terms of Saturation," *Concrete InFocus*, 2015, pp. 3-7.
46. Li, W.; Pour-Ghaz, M.; Castro, J.; and Weiss, J., "Water Absorption and Critical Degree of Saturation Relating to Freeze-Thaw Damage in Concrete Pavement Joints," *Journal of Materials in Civil Engineering*, ASCE, V. 24, No. 3, Mar. 2012, pp. 299-307. doi: 10.1061/(ASCE)MT.1943-5533.0000383
47. Weiss, W. J.; Ley, M. T.; Isgor, O. B.; and Van Dam, T., "Toward Performance Specifications for Concrete Durability: Using the Formation Factor for Corrosion and Critical Saturation for Freeze-Thaw," Transportation Research Board 96th Annual Meeting, Washington, DC, 2017, 20 pp.
48. Powers, T. C., "A Discussion of Cement Hydration in Relation to the Curing of Concrete," *Highway Research Board Proceedings*, V. 27, 1948, pp. 178-188.
49. ASTM C1585-13, "Standard Test Method for Measurement of Rate of Absorption of Water by Hydraulic-Cement Concretes," ASTM International, West Conshohocken, PA, 2013, 6 pp.
50. Vuorinen, J., "On Use of Dilation Factor and Degree of Saturation in Testing Concrete for Frost Resistance," *Nordisk Betong*, 1970, pp. 37-64.
51. Barde, V.; Radlinska, A.; Cohen, M.; and Weiss, W. J., "Relating Material Properties to Exposure Conditions for Predicting Service Life of Concrete Bridge Decks in Indiana," Report No. FHWA/IN/JTRP-2007/27, Joint Transportation Research Program, Purdue University, West Lafayette, IN, 2009, 218 pp.
52. Todak, H. N., "Durability Assessments of Concrete Using Electrical Properties and Acoustic Emission Testing," MSCE thesis, Purdue University, West Lafayette, IN, 2015.
53. Farnam, Y.; Bentz, D.; Hampton, A.; and Weiss, W. J., "Acoustic Emission and Low-Temperature Calorimetry Study of Freeze and Thaw Behavior in Cementitious Materials Exposed to Sodium Chloride Salt," *Transportation Research Record: Journal of the Transportation Research Board*, V. 2441, No. 1, Jan. 2014, pp. 81-90. doi: 10.3141/2441-11
54. Todak, H.; Tsui Chang, M.; Ley, M. T.; and Weiss, J., "Freeze-Thaw Resistance of Concrete: The Influence of Air Entrainment, Water to Cement Ratio, and Saturation," *Proceedings*, 11th International Symposium on Brittle Matrix Composites, Warsaw, Poland, 2015, pp. 101-109.
55. Kawamoto, S., and Williams, R. S., "Acoustic Emission and Acousto-Ultrasonic Techniques for Wood and Wood-Based Composites: A Review," General Technical Report No. FPL-GTR-134, United States Department of Agriculture, Washington, DC, 2002, 18 pp.
56. Tao, J.; Ghantous, R. M.; Jin, M.; and Weiss, J., "Influence of Silica Fume on Freezing-and-Thawing Resistance of Cement Paste at Early Age," *ACI Materials Journal*, V. 118, No. 2, Mar. 2021, pp. 107-116.
57. Jin, M.; Ghantous, R. M.; Tao, J.; and Weiss, J., "Freezing-and-Thawing Behavior of Cementitious Materials Containing Superabsorbent Polymers at Early Ages," *ACI Materials Journal*, V. 117, No. 6, Nov. 2020, pp. 243-252.
58. Ghantous, R. M.; Khanzadeh Moradillo, M.; Hall Becker, H.; Ley, M. T.; and Weiss, W. J., "Determining the Freeze-Thaw Performance of Mortar Samples Using Length Change Measurements during Freezing," *Cement and Concrete Composites*, V. 116, Feb. 2021, Article No. 103869.
59. Ghantous, R. M.; Madland, H.; Kwong, J.; and Weiss, W. J., "Examining the Influence of the Degree of Saturation on Length Change and Freeze-Thaw Damage," *Advances in Civil Engineering Materials*, V. 8, No. 1, 2019, pp. 365-374. doi: 10.1520/ACEM20190001
60. ASTM C150-07, "Standard Specification for Portland Cement," ASTM International, West Conshohocken, PA, 2007, 8 pp.
61. ASTM C494/C494M-08, "Standard Specification for Chemical Admixtures for Concrete," ASTM International, West Conshohocken, PA, 2008, 10 pp.
62. Greenspan, L., "Humidity Fixed Points of Binary Saturated Aqueous Solutions," *Journal of Research of the National Bureau of Standards, Section A: Physics and Chemistry*, V. 81A, No. 1, Jan.-Feb. 1977, pp. 89-96. doi: 10.6028/jres.081A.011
63. AASHTO TP 135-20, "Standard Method of Test for Determining the Total Pore Volume in Hardened Concrete Using Vacuum Saturation," American Association of State Highway and Transportation Officials, Washington, DC, 2020, 7 pp.
64. Bu, Y.; Spragg, R.; and Weiss, W. J., "Comparison of the Pore Volume in Concrete as Determined Using ASTM C642 and Vacuum Saturation," *Advances in Civil Engineering Materials*, V. 3, No. 1, 2014, pp. 308-315. doi: 10.1520/ACEM20130090
65. Trofimov, B. Y.; Kramar, L. Y.; and Schuldyakov, K. V., "On Deterioration Mechanism of Concrete Exposed to Freeze-Thaw Cycles," *IOP Conference Series: Materials Science and Engineering*, V. 262, 2017, Article No. 012019. doi: 10.1088/1757-899X/262/1/012019
66. Radlinska, A.; Rajabipour, F.; Bucher, B.; Henkensiefken, R.; Sant, G.; and Weiss, J., "Shrinkage Mitigation Strategies in Cementitious

Systems: A Closer Look at Differences in Sealed and Unsealed Behavior," *Transportation Research Record: Journal of the Transportation Research Board*, V. 2070, No. 1, Jan. 2008, pp. 59-67. doi: 10.3141/2070-08

67. Henkensiefken, R.; Bentz, D.; Nantung, T.; and Weiss, J., "Volume Change and Cracking in Internally Cured Mixtures Made with Saturated Lightweight Aggregate under Sealed and Unsealed Conditions," *Cement and Concrete Composites*, V. 31, No. 7, Aug. 2009, pp. 427-437. doi: 10.1016/j.cemconcomp.2009.04.003

68. Barrett, E. P.; Joyner, L. G.; and Halenda, P. P., "The Determination of Pore Volume and Area Distributions in Porous Substances. I. Computations from Nitrogen Isotherms," *Journal of the American Chemical Society*, V. 73, No. 1, Jan. 1951, pp. 373-380. doi: 10.1021/ja01145a126

69. Rajabipour, F., and Weiss, J., "Electrical Conductivity of Drying Cement Paste," *Materials and Structures*, V. 40, No. 10, Dec. 2007, pp. 1143-1160. doi: 10.1617/s11527-006-9211-z

70. Leão, T. P., and Tuller, M., "Relating Soil Specific Surface Area, Water Film Thickness, and Water Vapor Adsorption," *Water Resources Research*, V. 50, No. 10, Oct. 2014, pp. 7873-7885. doi: 10.1002/2013WR014941

71. Qiao, C.; Ni, W.; and Weiss, J., "Transport due to Diffusion, Drying, and Wicking in Concrete Containing a Shrinkage-Reducing Admixture," *Journal of Materials in Civil Engineering*, ASCE, V. 29, No. 9, Sept. 2017, p. 04017146. doi: 10.1061/(ASCE)MT.1943-5533.0001983

72. Esmaceli, H. S.; Farnam, Y.; Bentz, D. P.; Zavattieri, P. D.; and Weiss, W. J., "Numerical Simulation of the Freeze-Thaw Behavior of Mortar Containing Deicing Salt Solution," *Materials and Structures*, V. 50, No. 1, Feb. 2017, Article No. 96. doi: 10.1617/s11527-016-0964-8

73. de Wolski, S. C.; Bolander, J. E.; and Landis, E. N., "An In-Situ X-Ray Microtomography Study of Split Cylinder Fracture in Cement-Based Materials," *Experimental Mechanics*, V. 54, No. 7, Sept. 2014, pp. 1227-1235. doi: 10.1007/s11340-014-9875-1

74. Landis, E. N., and Keane, D. T., "X-Ray Microtomography," *Materials Characterization*, V. 61, No. 12, Dec. 2010, pp. 1305-1316. doi: 10.1016/j.matchar.2010.09.012

75. Nguyen, T. T.; Yvonne, J.; Bornert, M.; Chateau, C.; Bilteryst, F.; and Steib, E., "Large-Scale Simulations of Quasi-Brittle Microcracking in Realistic Highly Heterogeneous Microstructures Obtained from Micro CT Imaging," *Extreme Mechanics Letters*, V. 17, Nov. 2017, pp. 50-55. doi: 10.1016/j.eml.2017.09.013

76. Schneider, C. A.; Rasband, W. S.; and Eliceiri, K. W., "NIH Image to ImageJ: 25 Years of Image Analysis," *Nature Methods*, V. 9, No. 7, July 2012, pp. 671-675. doi: 10.1038/nmeth.2089

77. Scrivener, K. L.; Patel, H. H.; Pratt, P. L.; and Parrott, L. J., "Analysis of Phases in Cement Paste Using Backscattered Electron Images, Methanol Adsorption and Thermogravimetric Analysis," *MRS Online Proceedings Library*, V. 85, No. 1, Dec. 1986, Article No. 67.

78. McAndrew, A., "An Introduction to Digital Image Processing with MATLAB: Notes for SCM2511 Image Processing 1: Semester 1, 2004," School of Computer Science and Mathematics, Victoria University, Melbourne, VIC, Australia, 2004, 233 pp.

79. Beaudoin, J. J., and MacInnis, C., "Dimensional Changes of Hydrated Portland Cement Paste during Slow Cooling and Warming," *Cement and Concrete Research*, V. 2, No. 2, Mar. 1972, pp. 225-240. doi: 10.1016/0008-8846(72)90044-0

80. Meyers, S. L., "Thermal Expansion Characteristics of Hardened Cement Paste and of Concrete," *Highway Research Board Proceedings*, V. 30, 1951, pp. 193-203.

81. Mitchell, L. J., "Thermal Expansion Tests on Aggregates, Neat Cements, and Concretes," *ASTM International Proceedings*, V. 53, 1953, pp. 963-977.

82. Dettling, H., "Die Wärmedehnung des Zementsteines, der Gesteine und der Betone [Thermal Expansion of the Cement Paste, the Aggregates, and the Concretes]," thesis, Technische Hochschule Stuttgart, Stuttgart, Germany, 1962. (in German)

83. Emanuel, J. H., and Hulsey, J. L., "Prediction of the Thermal Coefficient of Expansion of Concrete," *ACI Journal Proceedings*, V. 74, No. 4, Apr. 1977, pp. 149-155.

84. Grasley, Z. C., and Lange, D. A., "Thermal Dilation and Internal Relative Humidity of Hardened Cement Paste," *Materials and Structures*, V. 40, No. 3, Apr. 2007, pp. 311-317. doi: 10.1617/s11527-006-9108-x

85. Sellevold, E. J., and Bjøntegaard, Ø., "Coefficient of Thermal Expansion of Cement Paste and Concrete: Mechanisms of Moisture Interaction," *Materials and Structures*, V. 39, No. 9, Nov. 2006, pp. 809-815. doi: 10.1617/s11527-006-9086-z

86. Powers, T. C., and Helmuth, R. A., "Theory of Volume Changes in Hardened Portland-Cement Paste during Freezing," *Highway Research Board Proceedings*, V. 32, 1953, pp. 285-297.

87. Coussy, O., *Poromechanics*, John Wiley & Sons, Inc., Hoboken, NJ, 2004.

88. Wang, Z. D.; Yao, Y.; and Wang, L., "Research on the Apparent Thermal Expansion Coefficient of Concrete Subject to Freeze-Thaw Cycles and Chloride Salt Attack," *Advanced Materials Research*, V. 446-449, 2012, pp. 3304-3310.

89. Powers, T. C., and Brownyard, T. L., "Studies of the Physical Properties of Hardened Portland Cement Paste," *ACI Journal Proceedings*, V. 43, No. 9, Nov. 1946, pp. 249-336.

90. Cai, H., and Liu, X., "Freeze-Thaw Durability of Concrete: Ice Formation Process in Pores," *Cement and Concrete Research*, V. 28, No. 9, Sept. 1998, pp. 1281-1287. doi: 10.1016/S0008-8846(98)00103-3

91. Scherer, G. W., and Valenza, J. J. II, "Mechanisms of Frost Damage," *Materials Science of Concrete VII*, F. Young and J. P. Skalny, eds., John Wiley & Sons, Inc., Hoboken, NJ, 2005, pp. 209-246.